



Using spherical indentation to measure the strength of copper-chromium-zirconium

Alexandra J. Cackett^{a,b,*}, Joven J.H. Lim^a, Przemysław Klupś^{a,b}, Andy J. Bushby^b, Christopher D. Hardie^a

^a CCFE, UK Atomic Energy Authority, Abingdon, Oxfordshire, OX14 3DB, UK

^b Queen Mary University of London, Mile End Road, London, E1 4NS, UK

HIGHLIGHTS

- The hardness of CuCrZr was measured using spherical nano-indentation.
- A strong indentation size effect was seen at low indentation strains.
- The indentation size effect was suppressed at higher strains.

ARTICLE INFO

Article history:

Received 15 December 2017

Received in revised form

5 March 2018

Accepted 6 April 2018

Available online 10 April 2018

Keywords:

CuCrZr alloy

ISE

Spherical indentation

ABSTRACT

Precipitation hardened CuCrZr will be used in heat-sink components in the ITER tokamak and is a primary candidate for EU DEMO. The measurement of mechanical properties of irradiated CuCrZr using conventional, standardised techniques is difficult due to the challenges involved in working with radioactive material and the relatively large specimen size required. Spherical nano-indentation offers a technique to measure stress-strain properties from far smaller volumes than conventional tests. In this work, CuCrZr has been heat-treated at different temperatures to vary the Cr precipitate size and spacing. Spherical nano-indentation using multiple tip radii was then used to produce stress-strain curves for all samples, from which values of initial flow stress were calculated. It was found that there was a strong indentation size effect (ISE) in the stress required to initiate plasticity, however at higher indentation strains the flow stress became constant for tip radii, $R, \geq 8 \mu\text{m}$. This suggests that at the initiation of plastic deformation the ISE is dominated by dislocation source activation but in later stages the interaction with microstructural material length-scales dominate the measured mechanical strength. The mechanical response of these small-scale tests is governed by multiple mechanisms, which convolute interpretation of data and must be considered when measuring the effects of irradiation on the mechanical properties.

Crown Copyright © 2018 Published by Elsevier B.V. All rights reserved.

1. Introduction

Due to its high thermal conductivity, high strength at elevated temperature, and commercial availability [1,2], precipitation hardened (PH) copper-chromium-zirconium (CuCrZr) alloy has for many years been used to make actively cooled plasma facing

* Corresponding author. Queen Mary University of London, Mile End Road, London, E1 4NS, UK.

E-mail addresses: alexandra.cackett@ukaea.uk (A.J. Cackett), joven.lim@ukaea.uk (J.J.H. Lim), p.klups@se13.qmul.ac.uk (P. Klupś), a.j.bushby@qmul.ac.uk (A.J. Bushby), chris.hardie@ukaea.uk (C.D. Hardie).

components in fusion reaction vessels [3]. To this effect, CuCrZr has also been selected as the heat-sink material for the International Thermonuclear Experimental Reactor (ITER) and is a primary candidate for EU DEMO and future power plants. The optimised chemical composition for ITER-grade CuCrZr specifies the alloying elements as being in the range 0.6–0.9 wt.% chromium and 0.07–0.15 wt.% zirconium with ≤ 0.15 wt.% impurities; peak strength is achieved by aging at $475 \text{ °C} \pm 5 \text{ °C}$ for 3 h [4]. When used for this purpose, the alloy response under neutron irradiation must be considered. As previously driven by the fission industry, small-scale testing techniques are preferred for neutron-irradiated material due to the induced radioactivity of samples and the

associated difficulty and cost in handling.

There are a range of small-scale experimental techniques that can be used to measure the mechanical properties of materials and investigate the mechanisms responsible for plastic deformation. Micro- and nano-pillar compression have extensively been used for this purpose [5–7], with in-situ studies providing additional information on fundamental processes such as slip step formation, and dislocation generation and movement [8,9]. Cantilever flexure is commonly used for experiments in fracture mechanics and cyclic fatigue [10–12]. Both these techniques require fabrication of miniaturised test pieces, typically carried out using a focussed ion beam (FIB), which can be expensive in terms of both time and facility costs, and data are subject to variation due to the current lack of a standardised approach for these techniques. One method that does not require intensive sample preparation is instrumented indentation testing (IIT), which is supported by ISO 14577 [13]. This technique is now highly automated and can perform a large number of tests in a short amount of time. Also, when sample size is limited (e.g. in thin films or ion-irradiated material), nano-indentation can be used to probe the very first few tens to hundreds of nanometres.

IIT using a spherical indenter tip has some advantages over using pointed indenters; due to the blunt geometry, spherical indentation can be initially elastic [14], therefore the whole strain range from elastic, elastic-plastic, and finally fully plastic deformation can be observed. This has made it possible to generate indentation stress-strain curves comparable to those from traditional tensile tests (see e.g. Refs. [15,16] and, more recently [17]). Results from indentation tests are, however, influenced by the indentation size effect (ISE), whereby the smaller the interaction volume between tip and sample the harder the material appears. The ISE has been the subject of many studies over the last two decades [18–21]. For Berkovich indentation, ISE is exhibited by a reduction in the measured hardness with an increase in penetration depth. For spherical indentation, the interaction volume and ISE are a function of both the tip radius and penetration depth, with a decrease in tip radii measuring a higher hardness. The extrinsic length-scale imposed by the test is directly related to this interaction volume and results in the commonly observed ISE; the underlying mechanisms responsible for this size effect in plasticity are yet to be fully understood and are a matter of debate [22].

Initial reasoning for the ISE was hypothesised by Fleck et al. [23] who suggested that since geometrically necessary dislocations (GNDs) are required for material deformation in a restricted volume, small indentations appear stronger because GND density scales with the plastic strain gradient, which is higher for smaller interaction volumes. This theory was later expressed by a model by Nix and Gao [24], which showed good agreement with experimental data for Berkovich indentation in Ag and Cu. However strain gradients cannot be the cause of all extrinsic size effects; for example, (perfect) uniaxial micro-pillars have no strain gradient yet still exhibit a 'smaller is stronger' behaviour [25]. There have since been many studies exploring further plasticity mechanisms that account for extrinsic size effects, which show that dislocation starvation and curvature also contribute to this phenomenon [26–29]. The fundamental mechanisms controlling the ISE are distinguished separately from the well-established strengthening due to microstructural intrinsic length-scales, e.g. grain size, obstacle spacing or film thickness [30–33].

In this work, indentation using spherical tips with a range of radii between 2 and 90 μm have been used to probe CuCrZr samples that have been heat-treated at different temperatures. The heat-treatments have the effect of changing the dominant internal length-scale of the material, in this case the average distance between Cr precipitates, which was characterised using transmission

electron microscopy (TEM). The aim of the study was to observe the effect of varying contributions from extrinsic and intrinsic length-scales on the observed size effect to give insights into the dominant mechanisms of dislocation plasticity in a PH alloy.

2. Material and methods

A 35 mm thick slab of Cu-1.0%Cr-0.06%Zr (wt%) in the solution annealed state (970 °C followed by water quenching) was divided into seven blocks; one block remained as-received (AR) and the other six were heat-treated for 2 h in a vacuum furnace at the following temperatures: 400, 480, 550, 600, 650, and 700 °C. Previous studies have already shown that fine, chromium-rich precipitates grow in size and the distance between them increases with higher aging temperatures [34,35], which is typical of PH alloys. The aim of the heat treatments was to generate a range of internal length-scales. Larger precipitates produced during solution annealing have also been identified in this ternary alloy (e.g. Cu₅Zr [36]), however they were not found to change after ageing heat treatments and subsequently are unlikely to be responsible for relative differences in hardness between ageing temperatures. A Leco LM-100 microindentation hardness tester was used to measure the Vickers hardness of the material after heat treatment. A load of 100gf was applied with a dwell time of 15s.

For nano-indentation, small samples were cut from each of the heat-treated blocks and mechanically polished with SiC abrasive paper down to a 2.5 μm grit size. They were then electropolished in a nitric acid and methanol 1:4 mix to produce a deformation-free flat surface. This electrolyte solution was also used to twin-jet polish 3 mm discs for observation in the TEM.

A Tescan MIRA3 FEG scanning electron microscope (SEM) was used to perform electron back-scatter diffraction (EBSD). The EBSD maps were then used to make grain size measurements using Channel5 software Tango, which used elliptic fits to the grains to calculate the geometric mean area and diameter. To measure precipitate size and spacing, a 200 kV FEI Talos scanning transmission electron microscope (STEM) was used. Bright- and dark-field micrographs were taken as well as chemical maps, which were acquired using the Super X-EDS (energy dispersive spectroscopy) system with four silicon drift detectors. Precipitate size and number density were calculated from the EDS maps using the particle analysis plugin in the software 'Fiji' [37].

Instrumented nano-indentation was performed using a Keysight G200 instrument with spherical tips of radii 2, 8, 15, 30, and 90 μm . Tip geometry as a function of indentation depth was determined via the calibration method described by Bushby and Jennett in Ref. [38], using reference samples of fused silica, sapphire, and glassy carbon. Indentation data was collected using a load-controlled, modified Field and Swain [39] approach with 40 load partial unload cycles per indent. Arrays consisting of a grid of 4 × 4 locations for the four smallest indenter tips and 3 × 3 for the largest, due to the increased area required to accommodate adequate spacing between indents, were run for each test. Indents were separated by a distance of greater than 10 times the final contact radius, a , of the indent impression.

3. Theory

The contact depth between sample surface and indenter tip was calculated using Hertzian contact mechanics [40]. Using the assumption that the unloading curve is purely elastic, Hertzian contact of a sphere and a concave residual impression can be described by the following equation:

$$h_e = \left(\frac{9}{16}\right)^{\frac{1}{3}} \left(\frac{F}{E^*}\right)^{\frac{2}{3}} \left(\frac{1}{R} - \frac{1}{R'}\right)^{\frac{1}{3}} \quad (1)$$

where F is the force applied, R is the tip radius and R' is the residual impression radius. E^* is the reduced modulus, defined as follows:

$$\frac{1}{E^*} = \frac{1 - \nu_i^2}{E_i} + \frac{1 - \nu_s^2}{E_s} \quad (2)$$

where E is Young's modulus, ν is Poisson's ratio, and the subscripts i and s refers to the indenter the surface respectively. The reduced radius, R^* , is similarly defined as,

$$\frac{1}{R^*} = \frac{1}{R_i} + \frac{1}{R_s} \quad (3)$$

The radius of the residual impression, h_r , is calculated on a per-cycle basis by extrapolating the unload curve back to the x-axis when the data is displayed on a load-displacement plot.

The contact radius between tip and surface, a , is simply a geometric relationship:

$$a = \sqrt{2R^*h_c - h_c^2} \quad (4)$$

Where the contact depth, h_c , is defined as

$$h_c = \frac{h_1 + h_r}{2} \quad (5)$$

with h_1 being the indentation depth at maximum load. Indentation strain and indentation stress can then be calculated using the following two expressions:

$$\epsilon = \frac{a}{R} \quad (6)$$

$$\sigma = \frac{F}{\pi a^2} \quad (7)$$

Indentation stress and strain are calculated for every cycle of the indentation, which finally produces a complete stress-strain curve that can be used to calculate a value of yield strength.

4. Results

The results of initial hardness testing using a Vickers indenter can be seen in Fig. 1, where each point represents an average of sixteen indents on each sample. This provided confirmation that a change in microstructural length-scale had the desired effect of altering the macroscopic hardness. The curve is typical of that of ageing of a PH alloy; peak strength is achieved when the material transforms from a solid solution to a fine distribution of coherent and semi-coherent precipitates with optimal spacing. This is then followed by a drop in strength due to coarsening of precipitates, increasing their size and decreasing their number density [41].

4.1. Microstructural characterisation

EBSD showed that the average grain size did not significantly change after any of the heat treatments were performed, with the AR sample having an average grain diameter of 74.5 μm (excluding $\Sigma 3$ twin boundaries).

Examples of background-subtracted Cr elemental maps obtained using STEM EDS are shown in Fig. 2(a)–(d). In the as-received material no obvious segregation of Cr was observed and

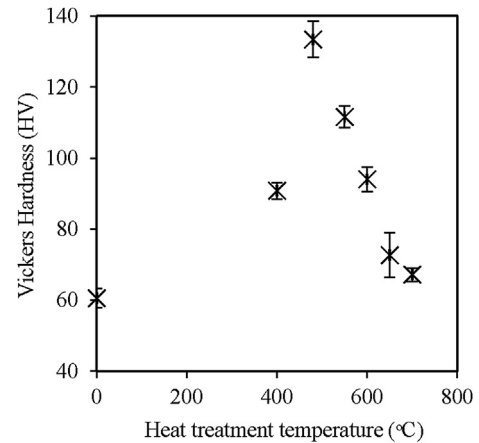


Fig. 1. Vickers hardness as a function of heat treatment temperature.

the Cr appeared to be homogeneously distributed in the sample. Heterogenous distributions of Cr were observed in the 400, 480 and 550 $^{\circ}\text{C}$ samples. Small clusters of Cr became visible in the 400 $^{\circ}\text{C}$ sample, as shown in Fig. 2(b). Discrete precipitates were first clearly observed in the prime-aged material that had been heat treated at 480 $^{\circ}\text{C}$ as shown in Fig. 2(g). They may have also been present in the 400 $^{\circ}\text{C}$ sample, however poor sample quality (oxidisation) obstructed the identification of fine features. Larger and more defined precipitates were found in the 550 $^{\circ}\text{C}$ sample and this trend of increasing precipitate size with higher heat-treatment temperature is indicative of the other samples aged at higher temperatures. Some of the precipitates were semi-coherent with the Cu matrix, as indicated by red circles in Fig. 2.

The results of Cr precipitate analysis using the EDS maps are summarised in Table 1 and shown graphically, to emphasise the overall trend, in Fig. 3. It was estimated that the areas observed by STEM were between 120 and 150 nm thick. The large variation in local thickness is due to the sample being produced via electro-polishing, hence it is difficult to ensure a homogeneous thickness across the specimen. Precipitate number density calculations were made based on this range and the EDS map area used for the analyses. Average precipitate diameter measurements were calculated using ellipse fits to each precipitate detected and represent the mean of the measured major and minor axes. These measurements confirm that a variation in internal length-scale has been achieved via systematically heat-treating at different temperatures.

Considering the above microstructural observations, indents are likely produced in a single grain or few grains, however the relatively smaller length-scale imposed by the precipitate structure (apart from the AR material) is considered to dominate the mechanical response of the indentation tests conducted in this study.

4.2. Spherical indentation

An example of load-displacement (after frame compliance and surface corrections) data, in this case for the as-received material and 2 μm tip, can be seen in Fig. 4. Deformation is initially elastic, as characterised by the loading and unloading points for each cycle being collinear, until a pop-in occurs. For subsequent cycles there is an offset in the load-unload curves, indicating that plastic deformation has taken place.

A plot of indentation stress versus indentation strain for the AR material, all indenter tips, can be seen in Fig. 5(a). As can be seen from the larger error bars, which here represent one standard deviation, data for the 2 μm tip was more scattered. This is likely due

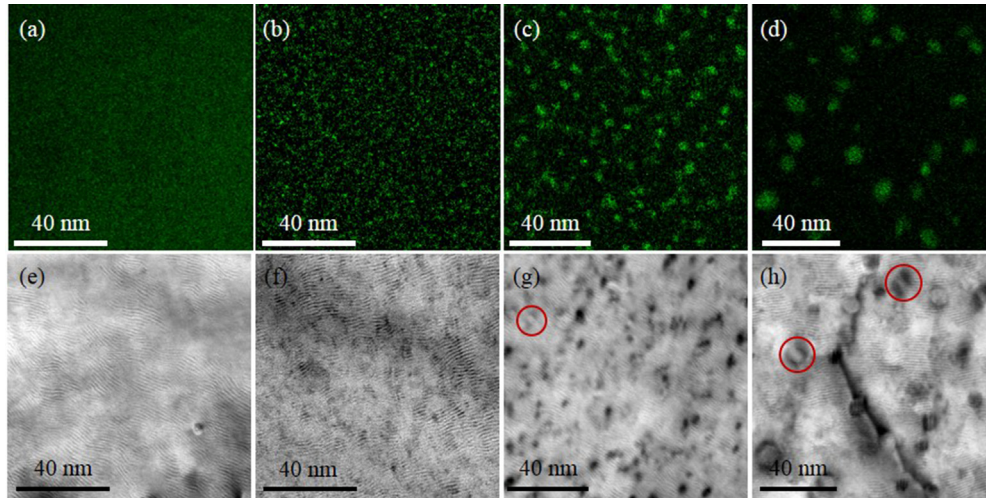


Fig. 2. (a)–(d) EDS chemical analysis Cr maps with (e)–(h) corresponding bright-field STEM micrographs for AR, 400 °C, 480 °C, and 550 °C heat treated CuCrZr respectively.

Table 1
Average precipitate diameter and number density for all samples.

Sample	Precipitate diameter (nm)	Precipitate density (m ⁻³)
AR	N/A	N/A
400	1.56	3.3–4.1 × 10 ²⁴
480	3.18	7.2–8.9 × 10 ²³
550	7.04	1.6–2.0 × 10 ²³
600	12.02	5.6–7.0 × 10 ²²
650	15.99	3.0–3.8 × 10 ²²
700	33.17	7.6–9.5 × 10 ²¹

to surface effects (e.g. contamination, hydration, inadequate surface finds, etc.) having a larger impact on contact area miscalculation when penetration depths are smaller. The elastic modulus is also affected by this, which exhibits as a systematic reduction in measured elastic modulus at low strain. An example of this can be seen in Fig. 5(b). The ISE is exhibited as higher hardness for smaller tip radii, however at high strains there is little variation between the responses from the largest four tips.

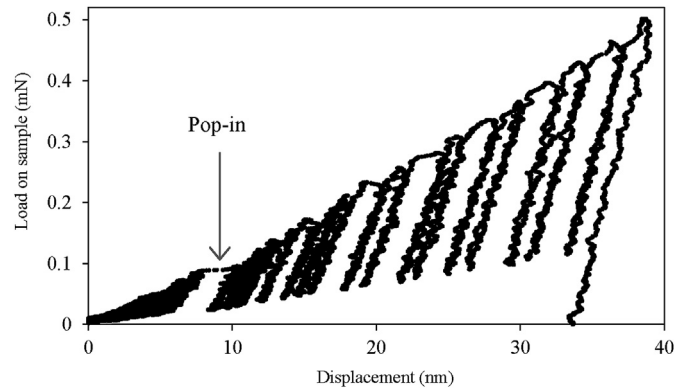


Fig. 4. Load-displacement graph for the as-received CuCrZr, 2 μm spherical tip.

The first data point of each interpolated and averaged data set was taken as a measure of initial flow stress. Furthermore, to compare the response of the material at the initiation of plastic

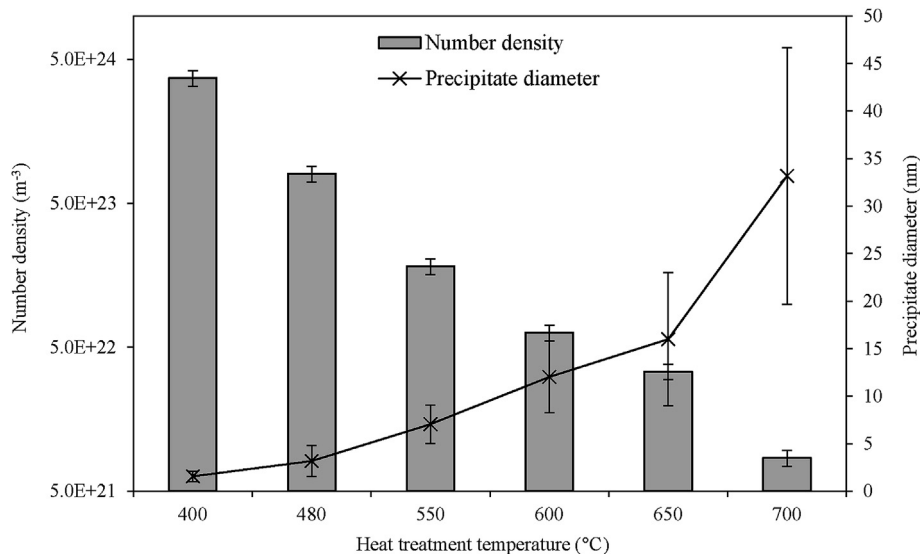


Fig. 3. Graphical representation of Cr precipitate number density (bars, logarithmic axis) and average diameter (line plot).

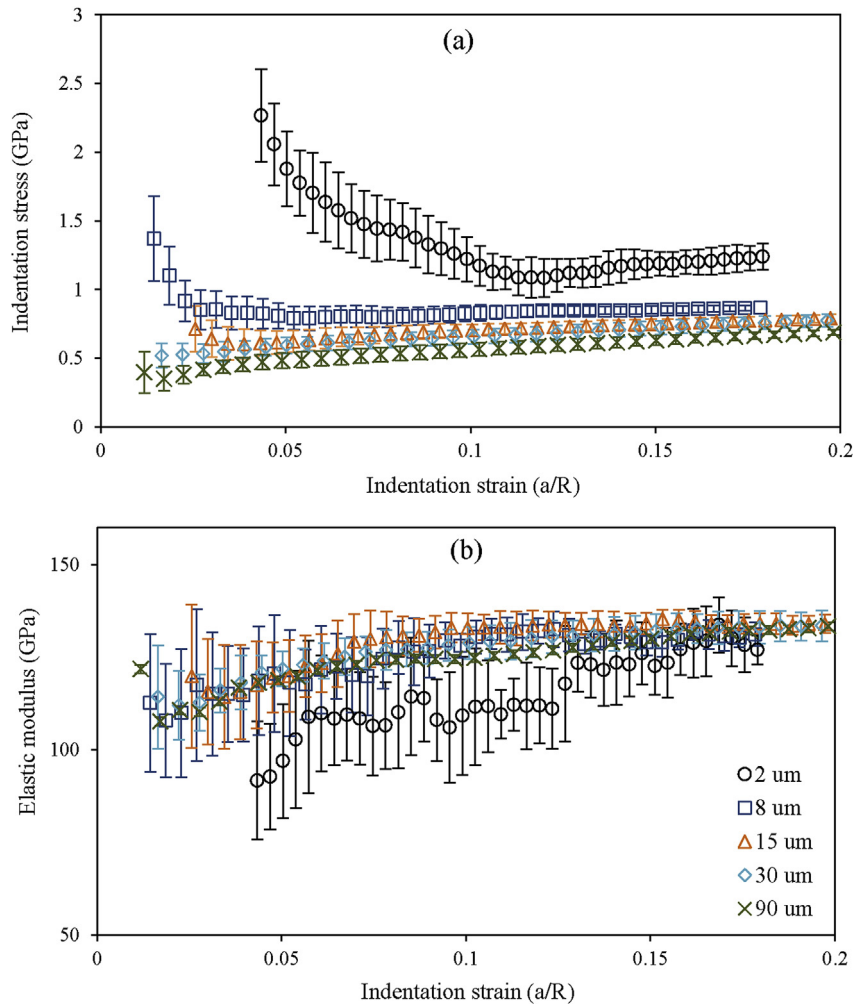


Fig. 5. Indentation results for AR (solution annealed) CuCrZr using five indenters of different radii; (a) indentation stress and (b) elastic modulus as a function of indentation strain.

deformation at low strains to stress measured at higher strains, additional measurements of stress were taken at values closest to $\epsilon = 0.15$ for each test. The results from these measurements, made on all samples with all indenter tips, can be seen in Fig. 6.

A pronounced ISE can be seen in Fig. 6(a), showing a decrease in initial flow stress with an increase in indenter tip radius for all tips from $R = 2$ – $90 \mu\text{m}$. There is not a great difference in this flow stress and ISE between all seven samples. A different result can be seen in Fig. 6(b), where the ISE appears to have little effect after an indenter radius of $8 \mu\text{m}$ but a clear intrinsic size effect can be seen throughout, which reflects that expected from the precipitate structure observed by TEM. It should be noted that it is not possible to fully rule out further slight decreases in hardness for tips larger than $R = 90 \mu\text{m}$, since this data is not available in the current study.

Fig. 7 compares the normalised hardness, with respect to that measured by the tip with a radius of $90 \mu\text{m}$ (H_{90}), with the inverse of tip radius for the CuCrZr material aged at 480C for 2 h. Measurements of stress at values closest to $\epsilon = 0.05$ have also been included; here it is easier to identify the gradual transition from a significant ISE observed at the initiation of flow stress, to smaller critical radii for minimal to no ISE.

The measurements of initial flow stress exhibit a particularly strong size effect and are all within the scatter of data for all samples. This suggests that the plastic flow stress near yield is independent of the comparative differences in the intrinsic length-

scale between samples and is dominated by the same mechanism for all materials. In contrast, the indentation stress measured at $\epsilon = 0.15$ appears relatively independent of indenter tip radii above $R = 8 \mu\text{m}$ and clear differences in flow stress are evident for the range of materials at this strain. Therefore, it is indicated here that the plastic response measured by these tests is dominated by the extrinsic length-scale at yield and transitions to a response influenced by intrinsic length-scale at higher strains; this transition strain is decreased with increasing tip radii. This may be explained by considering multiple size effect mechanisms influencing results. For example, on yield the response is dominated by dislocation source activation (i.e. starvation [42] or truncation [29]), which is more prominent with smaller tip radii due to a smaller interaction volume, and transitions to conventional dispersive barrier hardening once plasticity is fully established (e.g. at $\epsilon = 0.15$, as shown in Fig. 6(b)). As shown in Fig. 6(a), the measurement of initial flow stress between tips of $R = 30 \mu\text{m}$ and $R = 90 \mu\text{m}$ is consistent, suggesting that these ISE mechanisms are not present for the largest tip radii due to the relatively large interaction volume of these tests. These results are comparable to those produced from TEM in-situ pillar compression of proton-irradiated Cu [43] and, more recently, in ion-irradiated Fe-9%Cr ODS alloy [44], where yield strengths similar to macroscopic values were recorded from irradiated pillars of $\sim 400 \text{ nm}$ and $\sim 100 \text{ nm}$ respectively. The authors of the former of these conclude that below this value, “size-

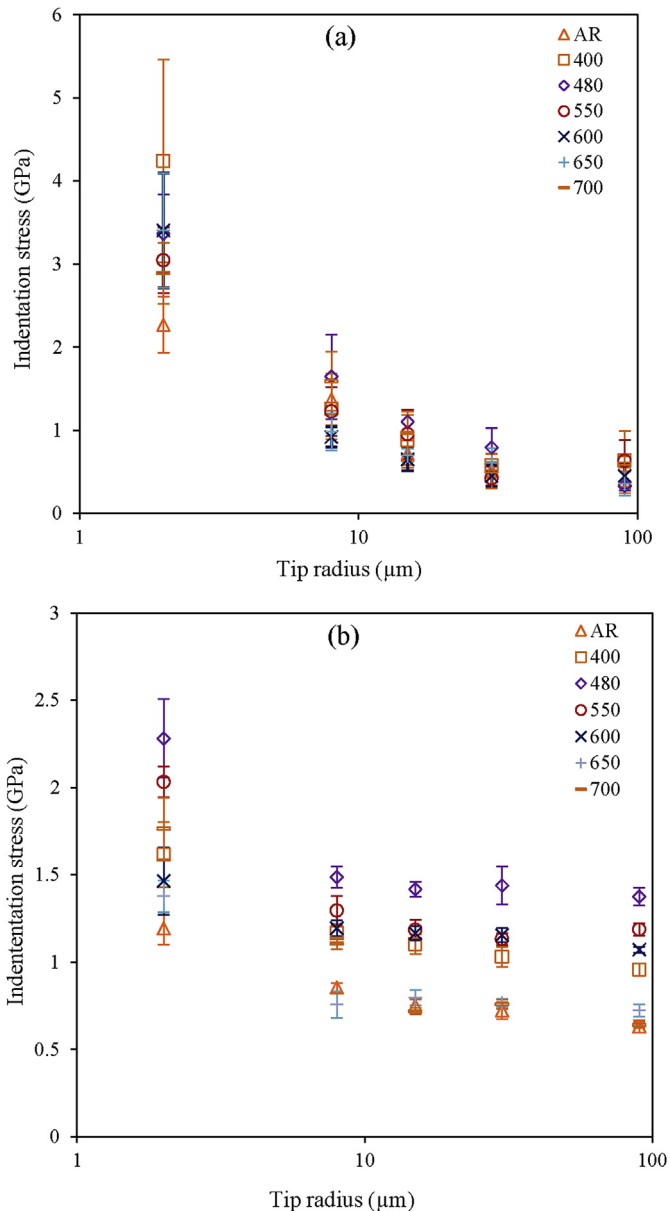


Fig. 6. Indentation stress calculated at (a) first available data point, and (b) 0.15 indentation strain.

dependent strength results from dislocation source limitation” as alluded to here. However, a larger interaction volume/length-scale threshold is observed in the current work, which is likely due to the larger obstacle spacing.

This concept requires substantiation by comparison of the experimentally observed data with available models regarding strain gradient plasticity and the dispersive barrier hardening model, to further understand the variation in mechanical response and associated mechanisms of dislocation plasticity. This is being conducted as part of future work.

5. Conclusions

By applying heat treatments to solution-annealed CuCrZr a variation in precipitate size and spacing can be achieved and, as the dominant intrinsic length-scale, greatly alters the hardness of the material. When tested using spherical nanoindentation with

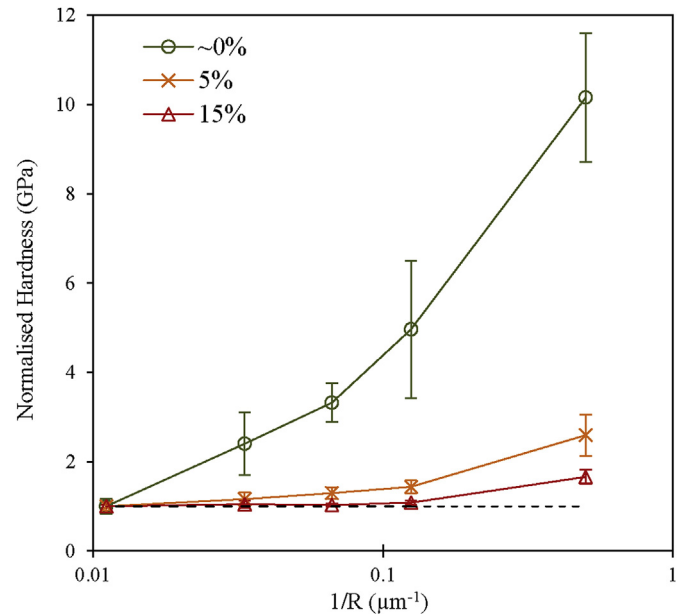


Fig. 7. Comparison of normalised hardness (H/H_{90}) versus the inverse of tip radii, showing the contribution of ISE relative to $R = 90 \mu\text{m}$ for strains of ~ 0 , 5 and 15% for tests in CuCrZr aged at 480°C for 2 h.

different tip radii an ISE in hardness is clearly observed in all samples. The observed size effect due to extrinsic length-scale (i.e. that imposed by external test geometry) is less apparent when testing with larger tip radii ($R > 8 \mu\text{m}$) and in the later stages of plastic deformation, where plasticity is well developed. This would indicate that once the interaction volume has grown to a critical size, the intrinsic length-scale is the dominant mechanism in resistance to plastic deformation, which is dislocation-precipitate interaction in these CuCrZr alloys. This suggests that opportunities to measure macroscopic mechanical properties may be obtained using spherical indenter tips in the range of \sim tens μm in this and similar alloys. In the case of irradiated material, where the dominant internal length-scale is altered by defects, the test piece size threshold may be reduced further still.

Declaration of interest

None.

Acknowledgements

This project has received funding from the EMPIR programme (14IND03) co-financed by the Participating States and from the European Union’s Horizon 2020 research and innovation programme. Equipment at the Materials Research Facility at UKAEA was used; the MRF is funded by the UK National Nuclear User Facility (EP/I037644/1) and Henry Royce Institute (EP/P021727/1). Thanks to the University of Manchester’s School of Materials for access to TEM facilities and support.

Appendix A. Supplementary data

Supplementary data related to this article can be found at <https://doi.org/10.1016/j.jnucmat.2018.04.012>.

References

- [1] A. Hernández-Pérez, M. Eddahbi, M.A. Monge, A. Munoz, B. Savoini,

- Microstructure and mechanical properties of an ITER-grade Cu-Cr-Zr alloy processed by equal channel angular pressing, *Fusion Eng. Des.* 98–99 (2015) 1978–1981, [https://doi.org/10.1016/S1003-6326\(11\)60986-2](https://doi.org/10.1016/S1003-6326(11)60986-2).
- [2] J.Y. Park, Y. Il Jung, B.-K. Choi, J.-S. Lee, Y.H. Jeong, B.G. Hong, Investigation on the microstructure and mechanical properties of CuCrZr after manufacturing thermal cycle for plasma facing component, *J. Nucl. Mater.* 417 (2011) 916–919, <https://doi.org/10.1016/j.jnucmat.2010.12.157>.
- [3] M. Lipa, A. Durocher, R. Tivey, T. Huber, B. Schedler, J. Weigert, The use of copper alloy CuCrZr as a structural material for actively cooled plasma facing and in vessel components, *Fusion Eng. Des.* 75–79 (2005) 469–473, <https://doi.org/10.1016/j.fusengdes.2005.06.056>.
- [4] V.R. Barabash, G.M. Kalinin, S.A. Fabritsiev, S.J. Zinkle, Specification of CuCrZr alloy properties after various thermo-mechanical treatments and design allowables including neutron irradiation effects, *J. Nucl. Mater.* 417 (2011) 904–907, <https://doi.org/10.1016/j.jnucmat.2010.12.158>.
- [5] M.D. Uchic, P.A. Shade, D.M. Dimiduk, Plasticity of micrometer-scale single crystals in compression, *Annu. Rev. Mater. Res.* 39 (2009) 361–386, <https://doi.org/10.1146/annurev-matsci-082908-145422>.
- [6] E.M. Grievson, D.E.J. Armstrong, S. Xu, S.G. Roberts, Compression of self-ion implanted iron micropillars, *J. Nucl. Mater.* (2012), <https://doi.org/10.1016/j.jnucmat.2012.06.014>.
- [7] D.M. Dimiduk, M.D. Uchic, T.A. Parthasarathy, Size-affected single-slip behavior of pure nickel microcrystals, *Acta Mater.* 53 (2005) 4065–4077, <https://doi.org/10.1016/j.actamat.2005.05.023>.
- [8] R. Fritz, D. Kiener, Development and application of a heated in-situ SEM micro-testing device, *Meas. J. Int. Meas. Confed* 110 (2017) 356–366, <https://doi.org/10.1016/j.measurement.2017.07.012>.
- [9] A.S. Schneider, D. Kiener, C.M. Yackacki, H.J. Maier, P.A. Gruber, N. Tamura, M. Kunz, A.M. Minor, C.P. Frick, Influence of bulk pre-straining on the size effect in nickel compression pillars, *Mater. Sci. Eng., A* 559 (2013) 147–158, <https://doi.org/10.1016/j.msea.2012.08.055>.
- [10] C. Motz, T. Schöberl, R. Pippan, Mechanical properties of micro-sized copper bending beams machined by the focused ion beam technique, *Acta Mater.* 53 (2005) 4269–4279, <https://doi.org/10.1016/j.actamat.2005.05.036>.
- [11] M.W. Kapp, T. Kremmer, C. Motz, B. Yang, R. Pippan, Structural instabilities during cyclic loading of ultrafine-grained copper studied with micro bending experiments, *Acta Mater.* 125 (2017) 351–358, <https://doi.org/10.1016/j.actamat.2016.11.040>.
- [12] J. Ast, M. Göken, K. Durst, Size-dependent fracture toughness of tungsten, *Acta Mater.* 138 (2017) 198–211, <https://doi.org/10.1016/j.actamat.2017.07.030>.
- [13] ISO Technical Committee ISO/TC 164/SC 3, 2016. ISO 14577 STANDARD.
- [14] T.T. Zhu, X.D. Hou, A.J. Bushby, D.J. Dunstan, Size effect at the initiation of plasticity for ceramics and metals, *J. Appl. Phys. D Appl. Phys.* 41 (2008), <https://doi.org/10.1088/0022-3727/41/7/074004>.
- [15] D. Tabor, *The Hardness of Metals*, Oxford, Clarendon Press, 1951.
- [16] F.M. Haggag, In-situ measurements of mechanical properties using novel automated ball indentation system, *ASTM Spec. Tech. Publ.* (1993) 27–44, <https://doi.org/10.1520/STP12719S>.
- [17] S. Pathak, S.R. Kalidindi, Spherical nanoindentation stress-strain curves, *Mater. Sci. Eng. R Rep.* 91 (2015) 1–36, <https://doi.org/10.1016/j.msner.2015.02.001>.
- [18] Y. Yee Lim, M.M. Chaudhri, The effect of the indenter load on the nanohardness of ductile metals: an experimental study on polycrystalline work-hardened and annealed oxygen-free copper, *Philos. Mag. A* 79 (1999) 2979–3000, <https://doi.org/10.1080/014186199251193>.
- [19] J. Swadener, The correlation of the indentation size effect measured with indenters of various shapes, *J. Mech. Phys. Solid.* 50 (2002) 681–694, [https://doi.org/10.1016/S0022-5096\(01\)00103-X](https://doi.org/10.1016/S0022-5096(01)00103-X).
- [20] A.J. Bushby, D.J. Dunstan, Plasticity size effects in nanoindentation, *J. Mater. Res.* 19 (2004) 137–142, <https://doi.org/10.1557/jmr.2004.19.1.137>.
- [21] G.M. Pharr, E.G. Herbert, Y. Gao, The indentation size effect: a critical examination of experimental observations and mechanistic interpretations, *Annu. Rev. Mater. Res.* 40 (2010) 271–292, <https://doi.org/10.1146/annurev-matsci-070909-104456>.
- [22] D.J. Dunstan, A.J. Bushby, Grain size dependence of the strength of metals: the Hall–Petch effect does not scale as the inverse square root of grain size, *Int. J. Plast.* 53 (2014) 56–65, <https://doi.org/10.1016/j.ijplas.2013.07.004>.
- [23] N. a Fleck, G.M. Muller, M.F. Ashby, J.W. Hutchinson, Strain gradient plasticity: theory and experiment, *Acta Metall. Mater.* 42 (1994) 475–487, [https://doi.org/10.1016/0956-7151\(94\)90502-9](https://doi.org/10.1016/0956-7151(94)90502-9).
- [24] W.D. Nix, H.J. Gao, Indentation size effects in crystalline materials: a law for strain gradient plasticity, *J. Mech. Phys. Solid.* 46 (1998) 411–425, [https://doi.org/10.1016/S0022-5096\(97\)00086-0](https://doi.org/10.1016/S0022-5096(97)00086-0).
- [25] J.R. Greer, W.C. Oliver, W.D. Nix, Size dependence of mechanical properties of gold at the micron scale in the absence of strain gradients, *Acta Mater.* 53 (2005) 1821–1830, <https://doi.org/10.1016/j.actamat.2004.12.031>.
- [26] T.T. Zhu, A.J. Bushby, D.J. Dunstan, Materials mechanical size effects: a review, *Mater. Technol.* 23 (2008) 193–209, <https://doi.org/10.1179/175355508X376843>.
- [27] O. Kraft, P.A. Gruber, R. Mönig, D. Weygand, Plasticity in confined dimensions, *Annu. Rev. Mater. Res.* 40 (2010) 293–317, <https://doi.org/10.1146/annurev-matsci-082908-145409>.
- [28] D.J. Dunstan, A.J. Bushby, The scaling exponent in the size effect of small scale plastic deformation, *Int. J. Plast.* 40 (2013) 152–162, <https://doi.org/10.1016/j.ijplas.2012.08.002>.
- [29] T.A. Parthasarathy, S.I. Rao, D.M. Dimiduk, M.D. Uchic, D.R. Trinkle, Contribution to size effect of yield strength from the stochastics of dislocation source lengths in finite samples, *Scripta Mater.* 56 (2007) 313–316, <https://doi.org/10.1016/j.scriptamat.2006.09.016>.
- [30] E.O. Hall, Deformation and ageing of mild steel: (III) discussion of results, *Proc. Phys. Soc. A* 64 (1951) 747–753.
- [31] J.M. Fragomeni, B.M. Hillberry, A micromechanical method for predicting the precipitation hardening response of particle strengthened alloys hardened by ordered precipitates, *Acta Mech.* 138 (1999) 185–210, <https://doi.org/10.1007/BF01291844>.
- [32] E.T. Lilleodden, W.D. Nix, Microstructural length-scale effects in the nano-indentation behavior of thin gold films, *Acta Mater.* 54 (2006) 1583–1593, <https://doi.org/10.1016/j.actamat.2005.11.025>.
- [33] X. Hou, N.M. Jennett, Application of a modified slip-distance theory to the indentation of single-crystal and polycrystalline copper to model the interactions between indentation size and structure size effects, *Acta Mater.* 60 (2012) 4128–4135, <https://doi.org/10.1016/j.actamat.2012.03.054>.
- [34] A. Chbihi, X. Sauvage, D. Blavette, Atomic scale investigation of Cr precipitation in copper, *Acta Mater.* 60 (2012) 4575–4585, <https://doi.org/10.1016/j.actamat.2012.01.038>.
- [35] D.J. Edwards, B.N. Singh, S. Tähtinen, Effect of heat treatments on precipitate microstructure and mechanical properties of a CuCrZr alloy, *J. Nucl. Mater.* 367–370 B (2007) 904–909, <https://doi.org/10.1016/j.jnucmat.2007.03.064>.
- [36] J.B. Correia, H.A. Davies, C.M. Sellars, Strengthening in rapidly solidified age hardened Cu-Cr and Cu-Cr-Zr alloys, *Acta Mater.* 45 (1997) 177–190, [https://doi.org/10.1016/S1359-6454\(96\)00142-5](https://doi.org/10.1016/S1359-6454(96)00142-5).
- [37] J. Schindelin, I. Arganda-Carreras, E. Frise, V. Kaynig, M. Longair, T. Pietzsch, S. Preibisch, C. Rueden, S. Saalfeld, B. Schmid, J.-Y. Tinevez, D.J. White, V. Hartenstein, K. Eliceiri, P. Tomancak, A. Cardona, Fiji: an open-source platform for biological-image analysis, *Nat Meth.* 9 (2012) 676–682, <https://doi.org/10.1038/nmeth.2019>.
- [38] A.J. Bushby, N.M. Jennett, Determining the area function of spherical indenters for nanoindentation, *MRS Proc.* 649 (2011), <https://doi.org/10.1557/PROC-649-Q7.17>.
- [39] J.S. Field, M.V. Swain, A simple predictive model for spherical indentation, *J. Mater. Res.* 8 (1993) 297–306, <https://doi.org/10.1557/jmr.1993.0297>.
- [40] H. Hertz, On the contact of rigid elastic solids, *J. Fur Die Reine Und Angew. Math* (1882), <https://doi.org/10.1515/crll.1882.92.156>.
- [41] D. Hull, D.J. Bacon, *Introduction to Dislocations*, 2011, <https://doi.org/10.1016/C2009-0-64358-0>.
- [42] W.D. Nix, J.R. Greer, G. Feng, E.T. Lilleodden, Deformation at the nanometer and micrometer length scales: effects of strain gradients and dislocation starvation, *Thin Solid Films* 515 (2007) 3152–3157, <https://doi.org/10.1016/j.tsf.2006.01.030>.
- [43] D. Kiener, P. Hosemann, S.A. Maloy, A.M. Minor, In situ nanocompression testing of irradiated copper, *Nat. Mater.* 10 (2011) 608–613, <https://doi.org/10.1038/nmat3055>.
- [44] K.H. Yano, M.J. Swenson, Y. Wu, J.P. Wharry, TEM in situ micropillar compression tests of ion irradiated oxide dispersion strengthened alloy, *J. Nucl. Mater.* 483 (2017) 107–120, <https://doi.org/10.1016/j.jnucmat.2016.10.049>.